Scale interactions between an internal seiche and double diffusion

N. Castro-Folker * and M. Stastna
Department of Applied Mathematics, University of Waterloo, Ontario N2L 3G1, Canada

(Received 2 June 2022; accepted 10 February 2023; published 7 March 2023)

We investigate the interaction between laboratory scale internal seiches and double-diffusive instabilities in the diffusive-convection regime using two-dimensional, high-resolution numerical simulations. A natural separation exists between the scale of the seiche and the scale of the mature instability. We report on how instabilities are modulated by, and how they modulate, the internal seiches. We find that seiche evolution leads to an earlier onset of instabilities compared to either an initially still fluid with a flat (i.e., seiche-free) interface, or an initially flat interface with an imposed stable shear current. We find that double-diffusion increases the buoyancy frequency and thereby decreases the period of the seiche. We interpret both mechanisms using existing internal wave theories. Additionally, we find that the combined viscous dissipation due to double-diffusive structures and shear stress induced by the seiche is greater than the viscous dissipation produced by either phenomenon in isolation. We discuss implications for more realistic configurations in which the internal seiche degenerates into a nonlinear internal wave train, how the observed mutual modulation may or may not manifest at the field scale, and how the full equation of state for sea water causes double-diffusive structures to grow asymmetrically in contrast to results using a linear equation of state.

DOI: 10.1103/PhysRevFluids.8.034801

I. INTRODUCTION

The ocean exhibits motion on scales that range from thousands of kilometers down to fractions of millimeters. Phenomena at these disparate scales interact to drive mixing, heat transport, and the ultimate dissipation of energy from large-scale forcing. A classic example of scale interaction is the energy cascade in the special case of an isotropic homogeneous, three-dimensional flow, where the transfer of kinetic energy from large scales to small scales via vortex stretching is described by Kolmogorov's five-thirds law [1]. This law is succinctly expressed in Fourier space as

$$E(k) \propto \epsilon^{2/3} k^{-5/3},$$

where $E(k)$ is the kinetic energy spectrum in the inertial subrange, ϵ is the rate of viscous dissipation, and k is the wave number (which is proportional to the inverse length-scale) [2]. While this law formally only applies to specific flows,[1] it expresses the general principle that large-scale features transfer energy in an inviscid manner to immediately smaller features. This process continues until the length-scales where viscosity and viscous dissipation dominate. Indeed, viscosity is believed to only play a role on these smallest scales.

Three examples of different classical theories of inviscid scale interactions are resonant wave-wave interactions, internal solitary wave-small wave interactions, and internal wave-eddy interactions. Internal waves can be represented by vectors in Fourier space. The interaction between

*ncastrof@uwaterloo.ca

[1]That is, it does not apply to the systems discussed in this investigation.

waves is then represented by a closed triad of these vectors; the wave with the largest vector in the triad transfers energy to the smaller waves [3]. This slow process of energy redistribution is believed to be continuously ongoing in the ocean interior, and is sometimes referred to as "wave turbulence" [4]. In coastal waters, a significant portion of the energy is found in internal solitary wave trains [5]. The highly nonlinear constituents of such wave trains, internal solitary waves, have been found to significantly damp the background field of small-scale internal waves [6] by subjecting them to a high shear environment that effectively disturbs their structure. In the ocean, internal waves co-exist with eddies of various size, and the interaction of such eddies and internal waves provides yet another example of interaction between scales. The study of these interactions has included numerical [7,8], and semi-analytical WKB [9,10] approaches. Theoretical approaches to wave-eddy interactions based on potential vorticity, typically in a simplified setting such as the shallow water equations, are ably surveyed by McIntyre [11].

Internal waves in confined settings (such as a laboratory tank, a basin, or a lake) can take a different form than those in the open ocean. Namely, these closed domains can contain internal standing waves known as internal seiches. Internal seiches are a widely observed aspect of lakes during the stratified season [12,13]. They are well studied experimentally [14–17], and aspects of their evolution have received attention from a numerical modeling point of view [18]. When they have a small amplitude, internal seiches are elementary standing waves. However, when their amplitude is larger, an initially standing internal wave will break down by one of several distinct mechanisms: (i) a combination of nonlinear steepening and dispersion can lead to the generation of propagating wave trains of solitary-like waves; (ii) the crests of an internal seiche may overturn and lead to large-scale mixing; (iii) at sufficiently strong shear levels, a Kelvin-Helmholtz instability sets in; or (iv) interactions with the bottom boundary layer may lead to the generation of local turbulent patches [12,18]. When the fluid density depends on temperature and salt there is a further possibility, namely the possibility of an interaction with double-diffusive instabilities. We explore this final example of an interaction between scales in this manuscript.

The density of seawater is a function of temperature and salinity, with larger values of salinity leading to larger values of density, and larger values of temperature leading to lower values of density. While both temperature and salinity are commonly represented by the same advection-diffusion equation, these quantities have vastly differing coefficients of diffusion (with that of salinity being two orders of magnitude lower than that of heat). This leads to a class of hydrodynamic instabilities generally called the double-diffusive instability, which comes in two varieties: the salt-finger regime, characterized by a stable temperature gradient opposed by an unstable salinity gradient; and the diffusive-convection regime, which is the reverse of the previous case [19,20]. Both varieties of instability lead to the formation of vortical, filament-like structures, which are on the order of centimetres in the ocean [20]. Oceanographers first discovered the activity of these (relatively) microscopic phenomena through the macroscopic currents that they deemed "the salt fountain" [21,22], and only later investigated the underlying, small-scale mechanisms [23]. Double diffusion has another macroscopic manifestation known as the thermohaline staircase: a layered stratification which may be several metres deep, and can persist laterally over O(100)km [24–26]. The exact formation mechanisms are still being actively investigated [20,27,28], but it is known that they contribute to large-scale fluxes of heat throughout the ocean. In fact, diffusive-convective thermohaline staircases contribute to the melting of sea ice by transporting heat from a deep intrusion of warm Atlantic water in the Arctic Ocean [29]. Shibley, Timmermans, *et al.* [24] report that the heat flux of the staircases depends on the thickness of layers, and the depth of the staircase itself; in turn, this suggests that internal waves with amplitudes on the order of the layer thickness could modulate the melting of ice by modulating the layer thickness.

In this manuscript, we report on laboratory scale simulations of internal seiches in a configuration that favours the development of double-diffusive instabilities in the diffusive-convection regime. Both the internal seiches and double-diffusive instabilities evolve naturally from a reasonably generic initial state and the separation of scales, while not the same as in the ocean, is sufficient to explore interactions between scales. We are thus able to study a nonlinear, multiscale system

with emergent properties, which is understood to be either a single component internal seiche, or a double-diffusive instability developing on its own. Our goal is to employ the scale separation between the large-scale internal seiches and small scale instabilities to analyze their mutual modulation, and demonstrate that this situation is realizable on laboratory scales.

The remainder of the manuscript is organized into three sections. The methods section, Sec. II, discusses the equations and software used to simulate the systems, and then discusses the details of the numerical experimental design. The section concludes with the discussion of a semianalytical model used to analyze the effect of double-diffusion on the seiche. Section III covers the results of the numerical experiments. This section is divided into three parts: first, the modulation of the double-diffusive instability by the seiche is discussed; next, the modulation of the seiche by the double diffusion and the resultant instabilities are discussed; and finally, the viscous dissipation of systems with and without double diffusion is discussed in detail (as such a comparison provides a clear picture of the mutual modulation between the seiche and the double-diffusive instability). Section IV is the discussion, where we describe a possible extension of our results to the field scale and how the nonlinearity of the equation of state for seawater introduces asymmetry to the growth of structures produced by double diffusion. The manuscript concludes in Sec. V with a summary of findings and several directions for future work.

II. METHODS

A. Governing equations and numerical methods

All simulations reported herein were performed using SPINS, a pseudospectral collocation solver for the stratified, incompressible Navier Stokes equations [30]. The pseudospectral collocation method results in the accuracy scaling with the number of grid points. An exponential filter is used to prevent the build-up of energy in the small length scales (i.e., aliasing).

The governing equations, under the Boussinesq approximation, with density-dependent on salinity and temperature read as follows:

$$\frac{D\vec{u}}{Dt} = -\frac{1}{\rho_0}\vec{\nabla}P - g\frac{\tilde{\rho}}{\rho_0}\hat{k} + \nu\nabla^2\vec{u}, \tag{1}$$

$$\vec{\nabla}\cdot\vec{u} = 0, \tag{2}$$

$$\frac{DT}{Dt} = \kappa_T\nabla^2 T, \tag{3}$$

$$\frac{DS}{Dt} = \kappa_S\nabla^2 S, \tag{4}$$

where the x axis points streamwise and is aligned with the flat tank bottom, the z axis points vertically and is aligned with the left wall of the tank. We denote the velocity by $\vec{u} = [u(x,z,t), w(x,z,t)]$, the density by $\rho(x,z,t)$, the temperature by $T(x,z,t)$, the salinity by $S(x,z,t)$, and the pressure by $P(x,z,t)$. The dimensions of the simulated tanks are L_x-by-L_z, and we use an N_x-by-N_z grid. Note that $\frac{D}{Dt}$ is the material derivative, which is defined as $\frac{D}{Dt} = \frac{\partial}{\partial t} + \vec{u}\cdot\vec{\nabla}$. We decompose the density as follows:

$$\rho = \rho_0 + \tilde{\rho}(x,z,t), \tag{5}$$

where $\tilde{\rho}$ represents fluctuations about a reference density, ρ_0. We apply the Boussinesq approximation; that is, variations in $\tilde{\rho}$ are due solely to changes in heat and salinity, ρ forces the momentum equation solely via $\tilde{\rho}$ in the buoyancy term, and

$$\left|\frac{\tilde{\rho}}{\rho_0}\right| \ll 1.$$

TABLE I. The coefficients for Eq. (6).

c_1	-9.20601×10^{-2}	kg m^{-3}
c_2	5.10768×10^{-2}	kg m^{-3} °C^{-1}
c_3	8.05999×10^{-1}	kg m^{3} PSU^{-1}
c_4	-7.40849×10^{-3}	kg m^{3} °C^{-2}
c_5	-3.01036×10^{-3}	kg m^{3} °C^{-1} PSU^{-1}
c_6	3.32267×10^{-5}	kg m^{3} °C^{-3}
c_7	3.21931×10^{-5}	kg m^{3} °C^{-2} PSU^{-1}

Keeping with convention, the momentum equation is divided by the constant reference density ρ_0, and the buoyancy term associated with the background density is balanced by the hydrostatic pressure. Hence, P represents the dynamic pressure. We use the following approximation to the UNESCO equation of state provided by Brydon *et al.* [31]:

$$\tilde{\rho}(x,z,t) = c_1 + c_2 T + c_3 S + c_4 T^2 + c_5 ST + c_6 T^3 + c_7 S T^2. \tag{6}$$

The coefficients are presented in Table I.

As shown by Özgökmen and Esenkov [32], a nonlinear equation of state will lead to asymmetries in the growth of the double diffusive structures in the salt finger regime. However, his theoretical calculations can be adapted to the regime in this investigation, and they show that the downward growing structures experience a greater buoyant force than the upward growing structures. Indeed, as will be seen in the results section, only downward growing structures are observed in the double-diffusive cases of this investigation.

Each case uses the following initial conditions for temperature and salinity:

$$T(x,z) = T_0 + \frac{\Delta T}{2}\left\{1 - \tanh\left[\frac{z - h_0 - 2a\cos\left(\frac{\pi x}{L_x}\right)}{b}\right]\right\}, \tag{7}$$

$$S(x,z) = S_0 + \frac{\Delta S}{2}\left\{1 - \tanh\left[\frac{z - h_0 - 2a\cos\left(\frac{\pi x}{L_x}\right)}{b}\right]\right\}. \tag{8}$$

These represent two layers separated by a thin, stratified interface that in the shape of a cosine (i.e., a standing internal wave). T_0 and S_0 are the temperature and salinity at the bottom of the tank (respectively), ΔT and ΔS are the vertical change in the temperature and the vertical change in the salinity (respectively), h_0 is the height of the thermocline and the halocline at $x = L_x/2$, and b is the width of the thermocline and the halocline; the values of these constants are presented in Table II. L_x and the half-amplitude of the initial disturbance in the thermocline and the halocline, a, are varied in this investigation. Their values are recorded in Table III. Additionally, the velocity fields were initialized with random perturbations to instigate the instabilities. Dn$_s$O is an exceptional case; it has periodic boundary conditions in x and a background velocity shear profile given by

$$U(z) = -u_0 \tanh\left(\frac{z - h_0}{b}\right), \tag{9}$$

where $u_0 = 0.0072$m/s. The parameters of this background shear current were chosen based on examination of cases with a seiche, so that the magnitude of the shear was representative of the

TABLE II. The constants of the initial conditions.

T_0	S_0	ΔT	ΔS	b
5°C	0 PSU	15 °C	6.0 PSU	1 cm

TABLE III. Parameters for each case. The cases are listed (from top to bottom) in the order of presentation in the text. A case name has three symbols: XYZ. X denotes the tank length. It can be S, D, or Q. S is for the original length case, D is for the double length case, and Q for the quadruple length case. Y denotes the amplitude, and the equilibrium position of the mixed layer. It can be A, a, S, or n. A is for the large amplitude case with the equilibrium at middepth, a is for the small amplitude case with the equilibrium at middepth, S is for the large amplitude case located above middepth, and n is for the zero-amplitude case located at middepth. Z denotes the parameters. It can be O, H, or S. O is for the oceanic/geophysical parameters, H is for κ_S increased to the oceanic κ_T, and S is for κ_T decreased to the oceanic κ_S. The exceptional supplemental case $\mathrm{Dn_sO}$ has an artificial initial shear given by Eq. (9). Note that in every case the viscosity is $\nu = 1.00 \times 10^{-6}\mathrm{m}^2 \times \mathrm{s}^{-1}$. The Pr and τ of the –O cases are similar to those of Lake Kivu and the order-of-magnitude estimates for the ocean cited by Radko [27].

Case	$N_x \times \mathrm{N}_z$	$L_x \times \mathrm{L}_z$ (cm × cm)	Pr	Sc	τ	a (cm)	h_0 (cm)
DnO	3072 ×768	51.2 ×12.8	6.99	100	6.99×10^{-2}	0.00	6.4
$\mathrm{Dn_sO}$	3072 ×768	51.2 ×12.8	6.99	100	6.99×10^{-2}	0.00	6.4
DAH	3072 ×768	25.6 ×12.8	6.99	6.99	1.00	2.50	6.4
DAO	3072 ×768	51.2 ×12.8	6.99	100	6.99×10^{-2}	2.50	6.4
QAO	6144 ×768	102.4 ×12.8	6.99	100	6.99×10^{-2}	2.50	6.4
SAO	1536 ×768	25.6 ×12.8	6.99	100	6.99×10^{-2}	2.50	6.4
SAH	1536 ×768	25.6 ×12.8	6.99	6.99	1.00	2.50	6.4
SAS	1536 ×768	25.6 ×12.8	100	100	1.00	2.50	6.4
SnO	1536 ×768	25.6 ×12.8	6.99	100	6.99×10^{-2}	0.00	6.4
SnH	1536 ×768	25.6 ×12.8	6.99	6.99	1.00	0.00	6.4
SaO	1536 ×768	25.6 ×12.8	6.99	100	6.99×10^{-2}	1.25	6.4
OSO	12 288 × 768	204.8 × 12.8	6.99	100	6.99×10^{-2}	2.50	9.6
OSH	12 288 × 768	204.8 × 12.8	6.99	6.99	1.00	2.50	9.6
OSS	12 288 × 768	204.8 × 12.8	100	100	1.00	2.50	9.6

value achieved over a portion of the seiche period (i.e., less than the peak value achieved due to the seiche).

The focal points of this investigation were the wave dynamics at the pycnocline, and the behavior of the structures produced by double diffusion, as opposed to detailed boundary layer dynamics. As such, free slip boundary conditions were imposed at the top and bottom of the domain. The boundaries of the domain were set to be impermeable to heat and matter, except in the case with the background shear for which the horizontal boundary conditions were periodic. Altogether, the systems mimicked the tilted-tank experiments typically used to study internal waves in laboratories.

B. Dimensionless parameters

Three dimensionless parameters are relevant for the analysis of the dynamics of the experiments. They are the Schmidt number, the Prandtl number, and the diffusivity ratio. The Schmidt number is defined as $\mathrm{Sc} = \frac{\nu}{\kappa_S}$, where κ_s is the diffusivity of salt, and ν is the kinematic viscosity. The Prandtl number is $\mathrm{Pr} = \frac{\nu}{\kappa_T}$ where κ_T is the diffusivity of heat. Lastly, the diffusivity ratio is simply $\tau = \frac{\kappa_S}{\kappa_T}$, and it determines if heat or salt is more diffusive in a given system. Thus, $\tau < 1$ is always true for a system with double-diffusive instabilities. These numbers were used to determine the most realistic sets of diffusivities, in the interest of creating qualitative results that could potentially be compared with experiments. For reference, Ref. [33] cites $\mathrm{Pr} = 6.25$, $\tau = 0.01$, and $\mathrm{Sc} = 625$ as values typical of Lake Kivu. Coincidentally, these are consistent with the order-of-magnitude summaries for oceanic values given by Ref. [27]: $\mathrm{Pr} \sim 10$, $\tau \sim 0.01$, and $\mathrm{Sc} \sim 100$.

Two other parameters are featured in other investigations of double-diffusion: the Rayleigh number, Ra, and the buoyancy ratio R_ρ. These are defined as

$$\mathrm{Ra} = \frac{g\alpha\Delta T H^3}{\rho_0 \nu \kappa_T}, \tag{10}$$

$$R_\rho = \frac{\beta\Delta S}{\alpha\Delta T}, \tag{11}$$

where H is a characteristic length scale, $\alpha = -\frac{\partial\rho}{\partial T}$ is the thermal expansion coefficient, $\beta = \frac{\partial\rho}{\partial S}$ is the haline contraction coefficient, and ΔT and ΔS are the instantaneous bulk differences in temperature and salinity across the characteristic length.

Ra and R_ρ can be used to measure the transport of heat across a thermohaline interface. Let Q be the convective heat flux; then, we can define the Nusselt number as $\mathrm{Nu} = \frac{Q}{\kappa_T \Delta T/H}$, where H is the width of the thermohaline interface. As discussed by Kelley *et al.* [28], a relationship of the form

$$\mathrm{Nu} \propto \mathrm{Ra}^p$$

can be used to estimate the convective heat flux across a thermohaline interface as follows:

$$Q \propto C(\alpha\Delta T)^{p+1},$$

where the empirical coefficient C is a function of R_ρ and p determines the power law. Turner [34] used dimensional analysis to determine $p = 1/3$, while Kelley *et al.* [35] find $p = 0.286$ to better agree with laboratory experiments in the range $\mathrm{Ra} = O(10^5)$–$O(10^9)$. Ra and R_ρ have also been used to determine and classify the stability of a double-diffusive system. For example, Fig. 4 of Carpenter *et al.* [36] presents stability diagrams in R_ρ-Ra space. The oscillatory diffusive-convection instability corresponds to the growth of anomalously dense (light) layers of fluid immediately below (above) the pycnocline.

In our present investigation, we have designed the unstable cases to produce diffusive-convection, and we are interested in how a large-scale phenomenon (the internal seiche) may interact with a small scale phenomenon (double-diffusive instabilities in the diffusive-convection regime). That is to say, we are not concerned with investigating flux laws or investigating stability conditions via an exhaustive parameter sweep. Rather, it is sufficient to use the first three dimensionless numbers to characterize our experiments, and it is sufficient to use qualitative analyses of the density field, quantitative analyses of the filtered kinetic energy, and quantitative analyses of a semianalytic linear model to describe and explain the results presented in Sec. III. Note that the aforementioned methods of analysis will be defined later in this section.

C. Experiments

This investigation is centered around three experiments, with a few supplemental cases used to clarify and motivate their results; the summary of all the cases is in Table III. The case names need some explanation. A case name has three symbols: XYZ. X denotes the tank length. It can take the values S, D, or Q. S is for the original length case, D is for the double length case, and Q for the quadruple length case. Y denotes the amplitude, and the equilibrium position of the mixed layer. It can take the values A, a, S, or n. A is for the original/large amplitude case with the equilibrium at middepth, a is for the small amplitude case with the equilibrium at middepth, S is for the large amplitude case located above middepth, and n is for the zero-amplitude case located at middepth. Z denotes the parameters. It can take the values O, H, or S. O is for the oceanic/geophysical parameters, H is for κ_S increased to oceanic κ_T, and S is for κ_T decreased to oceanic κ_S. The exceptional supplemental case $\mathrm{Dn_sO}$ has an artificial initial shear given by Eq. (9). This case key is reproduced in the caption of Table III.

Each case was simulated with the same resolution of approximately $r = L_x/N_x = L_z/N_z = 0.17$ mm. A fully resolved simulation of a thermohaline system requires the grid-scale to be smaller

than the scale of salinity variance dissipation [33,37]. One estimate of this is the Batchelor scale [37], which is given by

$$L_B = \left(\frac{\nu \kappa_S^2}{\langle \epsilon \rangle}\right)^{1/4},$$

where $\langle \cdot \rangle$ denotes the domain average and ϵ is the rate of viscous dissipation (ϵ is defined and discussed further in Sec. III C). This is analogous to the Kolmogorov scale for kinetic energy dissipation in a turbulent system [2]. Note that the Kolmogorov scale, η, is larger than L_B by a factor of $\sqrt{\mathrm{Sc}}$, which is a factor of 10 for the majority of cases in this investigation, and a factor of 2.64 for the rest (see Table III). As these quantities characterize the scales of dissipation in fully developed turbulence, they may not be representative of the dissipative scales in intermittent systems.[2] Flanagan *et al.* [38] instead use an estimate that they call the "double-diffusive" length scale:

$$L_S = \left(\frac{\rho_0 \nu \kappa_S^2}{g \kappa_T \left\langle \frac{\partial \rho}{\partial T} \frac{\partial T}{\partial z} \right\rangle}\right)^{1/4}.$$

Using post hoc calculations, we find that our systems satisfy, $0.02 < r/\eta < 0.57$, $0.24 < r/L_B < 5.69$, and $0.61 < r/L_S < 0.63$. Thus, our systems should have sufficient resolution for the analysis of all aspects of the velocity components, and for the analysis of trends in the scalar fields and the quantities derived from them. However, a detailed analysis of the energy and variance budgets, as derived by Hieronymus and Carpenter [37], would require a finer grid resolution.

Here we describe the three main experiments and the supplemental cases. In the first experiment we compare a nonlinear seiche with double-diffusive instabilities (SAO) to a nonlinear seiche with both scalars diffusing like heat (SAH) or salt (SAS); the latter two cases are effectively single-diffusive. In the second experiment we compare cases with different tank lengths, thereby varying the aspect ratio. The three cases used in this experiment are SAO, DAO, and QAO; they correspond, respectively, to the reference case, a double-length tank, and a quadruple-length tank. In the third experiment we focus on the effects of varying the initial amplitude across the cases; thus, we examine the evolution of the instabilities in the context of a nonlinear seiche (SAO), a linear seiche (SaO), and a still tank (SnO). At the start of Sec. III, we motivate the experiments by analyzing two supplemental cases with double diffusion and no seiche (DnO and $\mathrm{Dn_sO}$), and then analyzing one case with a seiche but no double diffusion (DAH). These cases consider the case of a stratification centered at the middepth. This is done to maintain standing wave behavior for as long as possible. When the stratification is centered away from the middepth internal seiches degenerate into nonlinear wave trains, such as those documented in Ref. [39]. Double diffusive effects on nonlinear internal wave trains are explored in a supplemental set of experiments, the results of which are presented in a subsection of the discussion (Sec. IV A).

D. Linear internal wave theory

Small amplitude internal seiches have a well developed linear theory, which provides a convenient means of categorizing the results of numerical experiments. In linear theory, the density is decomposed as

$$\tilde{\rho} = \rho_0[\bar{\rho}(z) + \rho'(x, z, t)], \tag{12}$$

where $\bar{\rho}(z)$ is the background density and ρ' is a small density perturbation due to the wave motion. Due to the incompressibility condition, the linearized governing equations can be written in terms

[2]That is, those systems where the local rate of viscous, salinity variance, or temperature variance dissipation do not equal the corresponding global rate.

of a stream function, ψ and the density perturbation ρ' as

$$(\nabla^2\psi)_t = \rho'_x g, \quad \rho'_t - \psi_x \bar{\rho}(z) = 0,$$

where subscript denote partial derivatives. Cross-differentiation then yields a single equation for the stream function

$$(\nabla^2\psi)_{tt} + N^2(z)\psi_{xx} = 0, \tag{13}$$

where $N^2(z) = -g\bar{\rho}(z)$ is the square of the so-called buoyancy frequency. The coefficients of this equation depend only on z. If we consider a rectangular domain with walls at $x = 0, L$, then the boundary condition of impermeable walls yields $u = \psi_z = 0$ and $w = 0$ at $z = 0, H$. This is easily converted to boundary conditions on the stream function, since

$$\psi_z = u, \quad \psi_x = -w.$$

Assuming a harmonic dependence in x and t allows us to write

$$\psi = \sum_n \sum_m a_n \phi_{m,n}(z) \sin(k_m x) \cos(\sigma_{n,m} t), \tag{14}$$

where m enumerates the horizontal modes, and n is enumerates the vertical modes. Specifically, the boundary conditions at $x = L$ yield the quantization condition

$$k_m = \frac{m\pi}{L}.$$

This quantization condition then informs the possible eigenvalues of

$$\sigma^2_{m,n}\phi_{zz} + (N^2(z) - \sigma^2_{m,n})k^2_m\phi = 0,$$

which is usually rewritten in terms of the "phase speed" $c_{m,n} = \sigma_{m,n}/k_m$,

$$\phi_{zz} + \left(\frac{N^2(z)}{c^2_{m,n}} - k^2_m\right)\phi = 0, \tag{15}$$

in analogy with the problem for horizontally propagating, linear internal waves. This equation follows from some straightforward algebra. This eigenvalue problem is solved for the vertical structure function $\phi_{m,n}$ and the frequency $\sigma_{m,n}$. Furthermore, Eq. (15) is a Sturm-Liouville problem. $c_{m,n}$ is maximum when $m = n = 1$ and decreases with both m and n. We will consider only the $m = 1$ case in our simulations, and hence will drop the subscript m in what follows. The detailed form of the vertical structure function depends on the form of $N^2(z)$, but general conclusions can be drawn due to the Sturm-Liouville form of the problem. Chief among these is that $c_1 > c_2 > c_3 > ...$ with corresponding $\phi_n(z)$ having $n - 1$ zeros on $0 < z < H$.

III. RESULTS

Our results are categorized into three sets of numerical experiments, and a collection of supplemental cases. We present the results of these experiments across three sections. First, we discuss how the seiche influences the growth of double-diffusive instabilities by qualitatively describing the growth of structures generated by the instabilities. Second, we discuss how double-diffusion affects the evolution of the seiche by noting its influence on the evolution of the internal wave.[3] Finally, we discuss the combined effects of the seiche and double diffusion on the viscous dissipation.

We suggest that readers view the accompanying videos in the Supplemental Material [40]. While they are supplemental, they convey dynamical details that static depictions are inherently unable to

[3]That is, the activation of the higher (larger values of n) vertical modes described in Sec. II D.

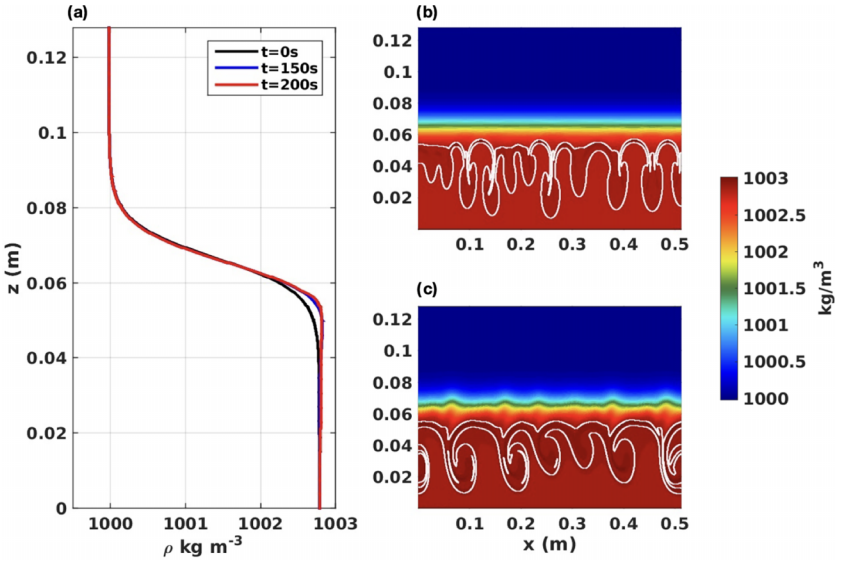

FIG. 1. (a) The evolution of the horizontal mean of density prior to the onset of mature double-diffusive instability DnO. (b) The density field at $t = 200$ s, the regions for which the density is larger than the maximum at $t = 0$s are enclosed in white contours, (c) the density field at $t = 200$ s, the regions for which the density is larger than the maximum at $t = 0$ s are enclosed in white contours, $\mathrm{Dn_sO}$.

represent. We will primarily reference the figures in this manuscript, but we will also mention when we believe the videos provide a deeper understanding.

To motivate and to provide context for the discussion of the interaction between internal seiches and double-diffusive instability, we briefly discuss the instability and seiche on their own. The results of two simulations with no seiche present, DnO and $\mathrm{Dn_sO}$, are shown in Fig. 1. Figure 1(a) shows the evolution of the horizontally averaged density profile due to double diffusion. A small region of statically unstable fluid develops near the bottom of the pycnocline, referred to as the *unstable boundary layer* [33,36], and leads to a mature instability with the structure of thin intrusions with mushroom-like caps [Fig. 1(b)]; in this paper we refer to these structures as filaments. Double diffusion leads to the generation of densities larger than the initial density maximum and in Figs. 1(b) and 1(c) these regions are enclosed in white contours. Figure 1(c) shows the mature state of the instability when a background shear current, initially given by Eq. (9), is present. It can be seen that the instabilities are now asymmetric, with the mushroom-like caps being replaced by billow-like caps. The horizontal spacing between mature instabilities is increased by roughly 60% relative to that of the no-shear (SnO) case.

The results of a case of a pure internal seiche evolution (i.e., without double-diffusive effects) is shown in Fig. 2. Figure 2(a) shows the spatiotemporal evolution of the vertically averaged kinetic energy. It can be seen that for early times ($t < 50$ s) the seiche is essentially a standing wave, however nonlinearity and dispersion lead to a modulation of the seiche shape soon after. Figure 2(b) shows the spectrum of the vertically averaged kinetic energy.[4] A logarithmic scale is used, and clearly shows that the seiche remains coherent as a first mode seiche in the horizontal for all times. Higher wave numbers are activated by the nonlinear evolution, reaching a peak around $t = 75$ s. The mode-1 structure in the vertical dominates the form of the seiche, and hence there is significant shear and viscous dissipation, across the pycnocline. This means that the seiche-induced kinetic

[4]Note that this is not the same quantity as the kinetic energy spectrum of turbulence theory.

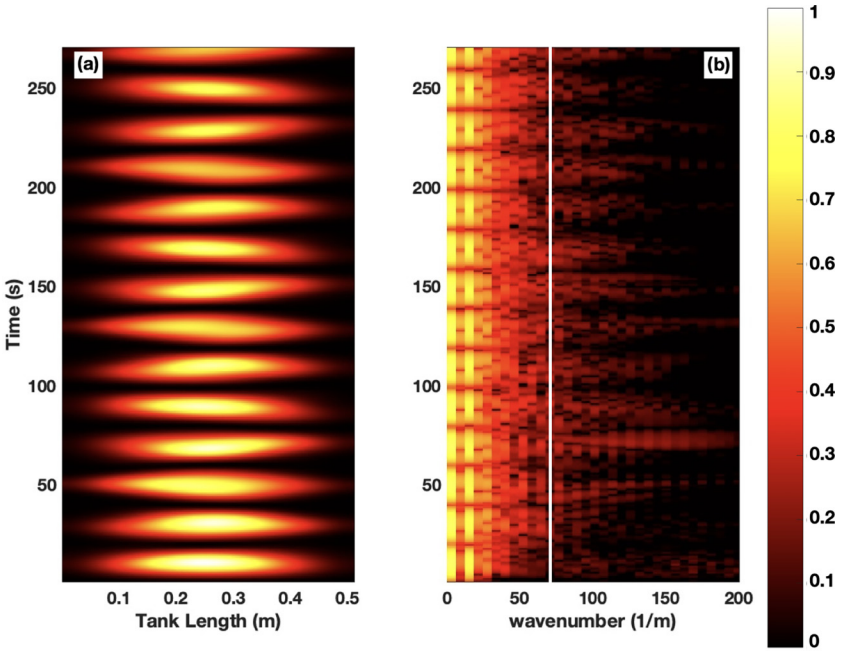

FIG. 2. (a) The evolution of the vertical mean of kinetic energy as a function of x and t for a seiche without double-diffusive effects; case DAH. (b) The base-10 logarithm of the spectrum of the vertical mean of kinetic energy as a function of k and t; the white bar denotes the cutoff k for the high-pass filter. Both panels are normalized by their respective maxima.

energy spectrum evolves due to a relatively complex interplay between nonlinear steepening and dissipation. Nevertheless, nonlinear effects will move some of the seiche's kinetic energy to wave numbers that characterized the double diffusive instability in the seiche-free case (Fig. 1).

Internal seiches in a double-diffusive system thus provide a dynamic environment in which the double-diffusive instability develops. In particular, by inducing a horizontally changing stratification, as well as spatiotemporal changes in the background shear current. Moreover, actual (as opposed to theoretical) internal seiches exhibit a structure that is multimodal in both the horizontal (due to nonlinear effects) and vertical (due to the fact that real world initial conditions do not project onto only one vertical mode). Nevertheless, due to the large (relative to the scale of initial double-diffusive structures) horizontal extent of seiches, it is expected that the interaction between internal seiches and the developing instabilities will exhibit scale separation. That is, it should be possible to select a cutoff length scale between initial representative scales of the seiche and the instabilities, therefore allowing for a quantitative analysis of the modulation of the double-diffusive instability by the seiche (and *vice-versa*) via filtering.

A. Modulation of double diffusion by the seiche

The evolution of the double-diffusive instability with and without a seiche can be compared quantitatively using the spectrum of the vertically averaged kinetic energy. Specifically, we consider the spectrum integrated over a range of wave numbers corresponding to activity generated by the double-diffusive instability without shear. Figure 3 compares cases with varying aspect ratios—SAO, DAO, and QAO—to a case without a seiche, DnO. The maximum of DnO has been chosen as the scaling factor, so that values exceeding 1 indicate a spectral power larger than the maximum of the pure double-diffusive instability. The cutoff for the high-pass filter was selected to best isolate the KE signals of double diffusion from those of the seiche; for example, at this cutoff the maximum

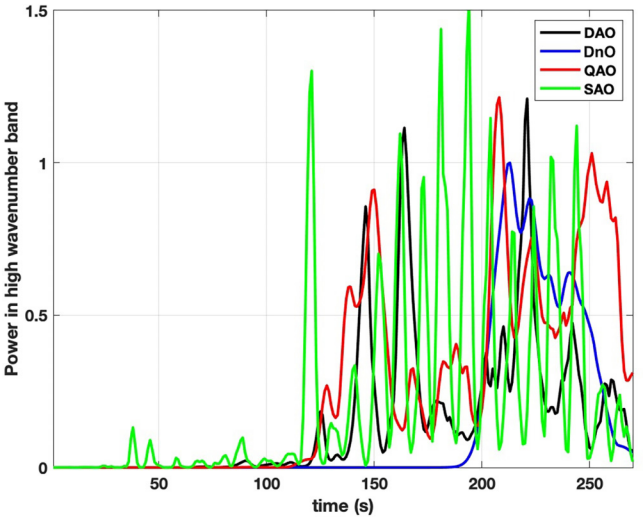

FIG. 3. The evolution of the spectrum of the vertical mean of kinetic energy integrated over the range $73.63\ \mathrm{m}^{-1} < k < 18\,850\ \mathrm{m}^{-1}$ as a function of x and t. Note that the signal of DnO is unfiltered, since there is no seiche present in this case. All curves have been scaled by the maximum of case DnO ($8.74 \times 10^{-7}\mathrm{m}^2/\mathrm{s}^2$), or in other words of double-diffusive instability without a seiche (blue line).

of the high-pass KE of SAH is approximately 2% the maximum of the high-pass KE of SnO.[5] The upper bound on the high-pass power band is imposed by the Nyquist wave number.

Several facts can be immediately gleaned from Fig. 3:

(1) The presence of the seiche leads to an earlier onset of the instability.

(2) All cases with a seiche exhibit a higher maximum spectral power than the case with only the double-diffusive instability (DnO).

(3) For the largest aspect ratio (i.e., shortest tank) the signal follows the period of the seiche.

(4) For smaller aspect ratios the signal has structure at the period of the seiche, but more complex temporal behavior is observed (consistent with a complex interplay between nonlinearity and dispersion).

To better understand the impact of the seiche on the double-diffusive instability refer to Figs. 4 and 5, which show samples of the density field at $t = 130$ s and $t = 225$ s, respectively. Note that the fields in Fig. 4 were sampled before the onset of the double-diffusive instability.[6] Figure 4(a) shows a large filament near the right wall for case SAO. This is due to the formation of a pycnocline bulge, or a mode-2 wave, near the boundary. Figures 4(b) and 4(c) show intermittent double-diffusive instabilities in the near-wall regions (though not necessarily immediately adjacent to the walls) for cases DAO and QAO, respectively. In all cases the central, near-node, region of the domain exhibits no double-diffusive instability. These distributions can be explained by the dispersion of the seiche. As the seiche evolves, it degenerates into smaller-scale waves, some of which are localized mode-2 disturbances that bulge or pinch the pycnocline. For example, during the initial evolution of every seiche centered at middepth, a bulge is observed in the center third of the tank (a visual example is available in the supplementary material). These disturbances can locally increase or decrease the interface width, and in turn locally modulate the rate of formation of the unstable boundary layer. Furthermore, both the currents and the mode-2 waves generated by the seiche can distend the unstable boundary and trigger the generation of a filament. Stamp *et al.* [41] noticed

[5]For this reason, -AH and -AS signals are omitted from Fig. 3.

[6]The onset occurs at approximately $t = 190$ s, according to the DnO signal in Fig. 3.

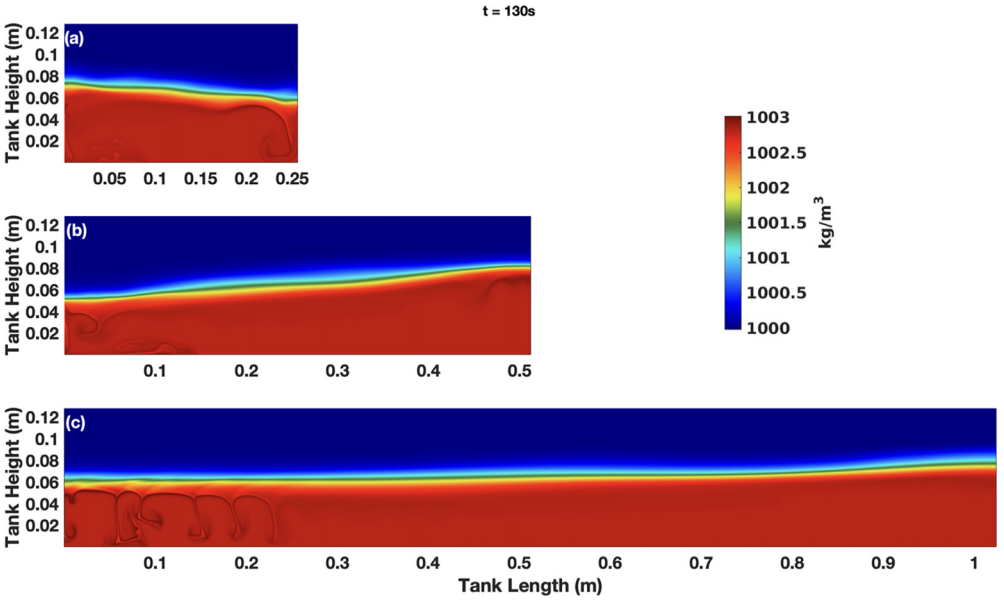

FIG. 4. The density field at $t = 130$ s as the aspect ratio of the domain is varied. (a) SAO, (b) DAO, (c) QAO.

a similar modulation of double diffusive instabilities in the diffusive convection regime, although the (disparately smaller) mode-2 waves he studied were generated by the circulating motions of filaments in the late evolution of double-diffusive instabilities.

Figure 5 shows the density field after the double-diffusive instability has manifested everywhere in the domain. In Fig. 5(a) a mode-2 wave is evident in the main pycnocline. The smaller apsect

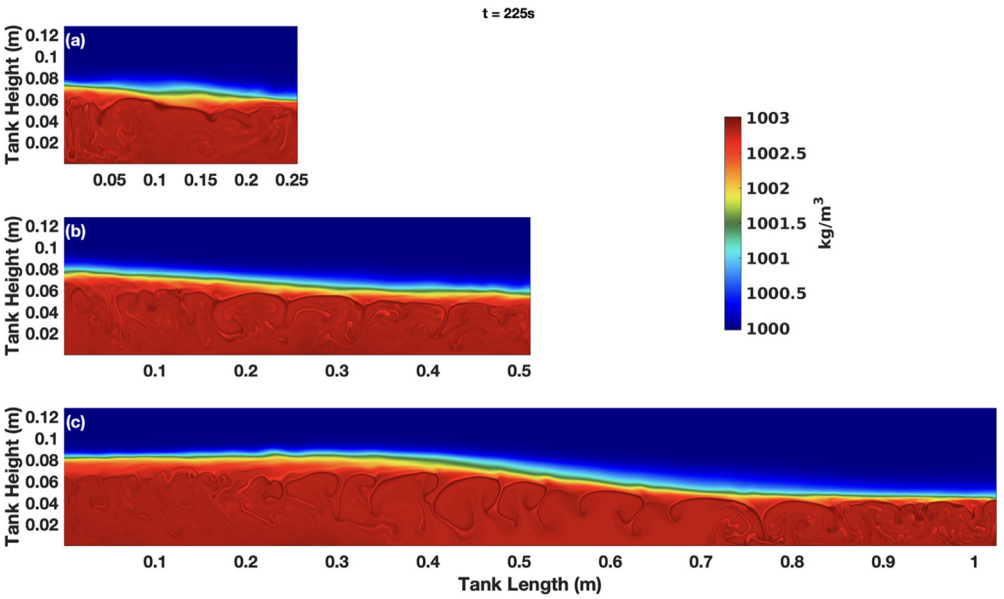

FIG. 5. The density field at $t = 225$ s as the aspect ratio of the domain is varied. (a) SAO, (b) DAO, (c) QAO.

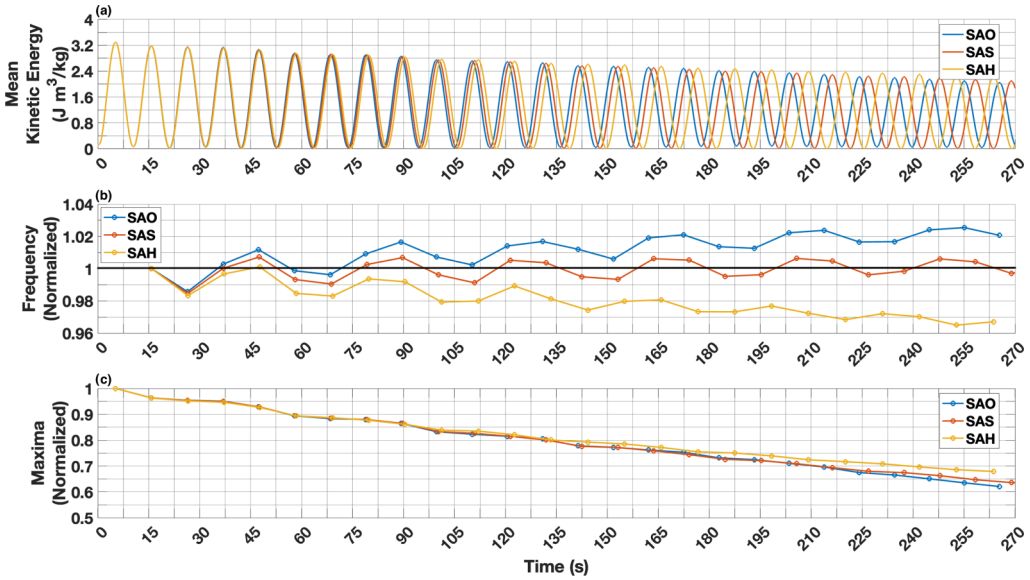

FIG. 6. Panel (a) is the mean kinetic energy (MKE) of the SAO, SAH, and SAS cases, panel (b) is a comparison of the period of each MKE signal, and panel (c) is a comparison of the maxima of each MKE signal. In all cases the time grid is equal to the set of times corresponding to the local maxima of the MKE signal for SAH. The time series in panels (b) and (c) are normalized by their initial values: the initial period of SAO is 10.53 s, the initial period of SAH is 10.56 s, and the initial period of SAS is 10.54 s; the initial maximum KE of all cases is 3.300×10^{-4} J $\times$ m^3/kg. The period signal was calculated by subtracting the time of the nth maximum from the $(n+1)$th maximum, and assigning this value to the time of the $(n+1)$th maximum. As well, the black bar in panel (b) marks the initial value for all series in this panel. As can be seen in panel (b), the seiche in SAO completed 25 oscillations in 265 s, in SAH completed 24 oscillation in 264 s, and in SAS completed 25 oscillations in 269 s. The net decreases in panel (c) are 37.9% for SAO, 36.4% for SAS, and 32.1% for SAH.

ratio cases in Figs. 5(b) and 5(c) clearly show that the funnel-like shape of the instability occurs consistently across the simulated tank, with evidence of advection by the seiche-induced currents closer to the bottom of the domain. Because the presence of the seiche leads to an earlier onset of the instability, the mature instabilities shown in Fig. 5 propagate into an environment that contains the remnants of previously formed instabilities.

B. Modulation of the seiche by double diffusion

We next consider how the presence of the instability affects the evolution of the internal seiche. The rate of modulation of the seiche should be commensurate with the timescale of the growth of the instabilities; thus, the observed slow growth of the instabilities suggests that the instability-induced changes should be similarly gradual.[7] Figure 6(a) shows the time series of the domain-integrated kinetic energy for the case with double diffusion SAO, as well as two cases without double diffusion. SAH (SAS) sets both the κ_T and κ_S to the κ_T (κ_S) used in case SAO. It can be seen that the total kinetic energy gradually decays in all cases. The oscillations of the three cases are in phase for $t < 70$ s, but beyond this a gradual decoherence is observed. Figure 6(b) extracts the period of

[7]If the parameter regime allowed for a greater κ_S and κ_T, then the growth time would be shorter, and the changes in the seiche would also be faster.

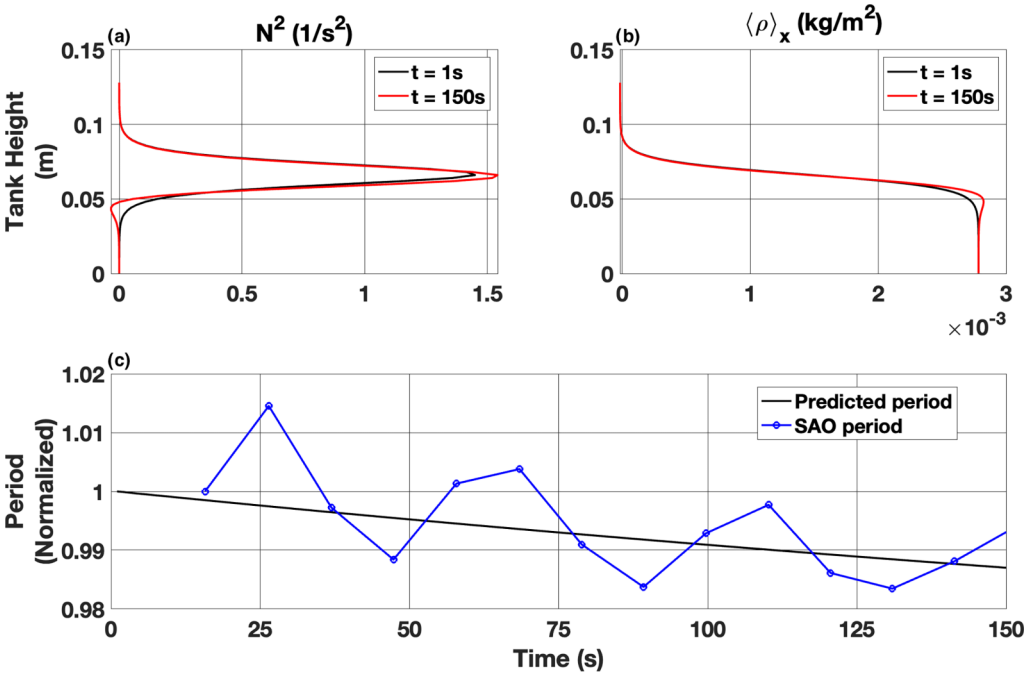

FIG. 7. The evolution of the vertical structure of a fluid with the same stratification as case SnO; i.e., $N^2(z,t)$ is calculated using $\langle\rho_{\text{SnO}}\rangle_x$ as the vertical background stratification; it is then used to calculate linear wave period at each time. Panel (a) is a plot of $N^2(z,t)$ at $t = 1$ s and $t = 150$ s, panel b) is a plot of the horizontally averaged density ($\langle\rho_{\text{SnO}}\rangle_x$) at $t = 1$ s and $t = 150$ s, and panel c) is a plot of the time series of the linear wave period for the first mode calculated using Eq. (15) with a wave number $k = 12.3$ m^{-1} (the wave number corresponding to the scale of the seiche in SAO), and the time series of the period of the seiche in SAO; the time series in panel (c) are normalized by their initial values, so they each represent a relative change in period. Note that relative change in the linear mode-1 internal wave period acts as a "line of best fit" for the relative change in the period of SAO.

oscillations as a function of time, and somewhat surprisingly shows qualitatively different behavior in all three cases. Case SAS largely maintains its initial period, case SAH exhibits a period that increases, while the double-diffusive case SAO exhibits a period that decreases. The two cases without double diffusion can be readily understood via the linear wave theory described in Sec. II D. For SAS the very low value of salt diffusivity means that the $N^2(z)$ profile remains essentially unchanged over the simulation time. In contrast, the higher diffusivity of the SAH case broadens the $N^2(z)$ profile slightly while decreasing its peak value, yielding a smaller c_1 and hence a longer period. To understand why the SAO case yields a shorter seiche period we extract the horizontally averaged density profile from SnO and SnH, numerically differentiate the density profile to obtain a time-dependent $N^2(z,t)$ profile, and numerically solve the resulting linear eigenvalue problem given by Eq. (15) at each time. Figure 7 shows the results of this procedure for SnO, and Fig. 8 shows the same for SnH. For panels (a) and (b) of Figs. 7 and 8, two times were selected as representative: $t = 1$ s and $t = 150$ s, where the former is representative of initial/early time conditions, and the latter of the conditions at a time just prior to the onset of double-diffusive instability throughout the domain. Panel (a) shows the $N^2(z,t)$ which is used in the eigenvalue problem solver, and panel (b) shows the density profile. In the SnO case, it can be seen that the primary effect of double diffusion is to create a region of anomalously high density at the bottom of the pycnocline, so that locally more dense fluid overlies less dense fluid (i.e., static—or Rayleigh-Taylor—instability). This is reflected in a small region over which $N^2 < 0$. Additionally, as can be seen in panel (b), this local density

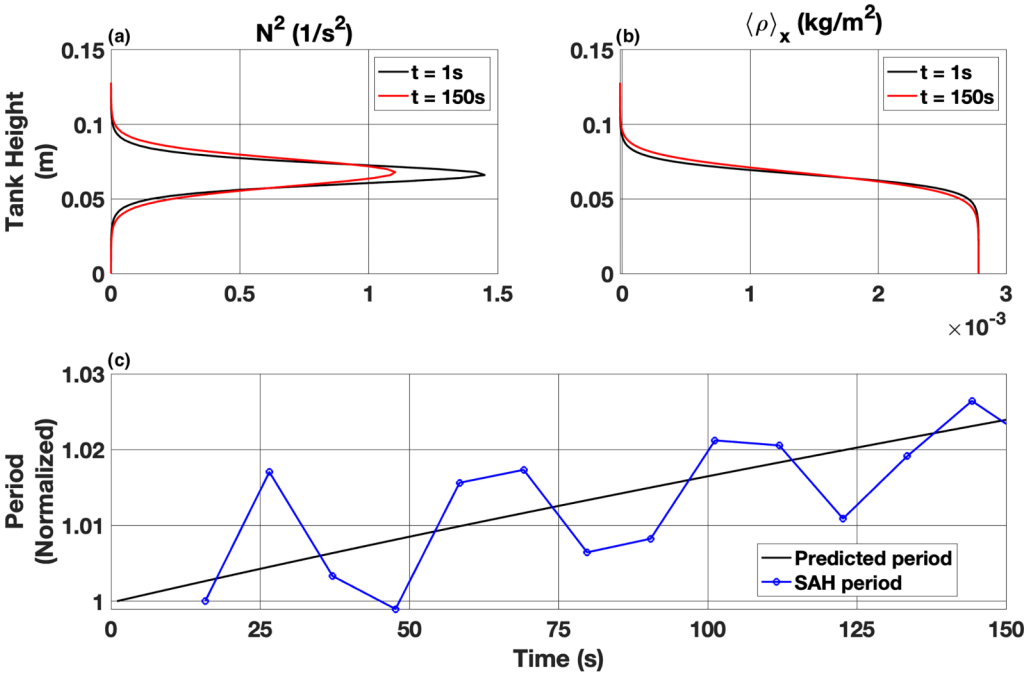

FIG. 8. Same as described in the caption of Fig. 7, but for case SnH.

anomaly creates a greater transition over the pycnocline which, causes the peak of N^2 to increase from time $t = 1$ s to $t = 150$ s. In contrast, Fig. 8(b) shows that single diffusion leads to a broader pycnocline, which in turn causes the N^2 profile to broaden and its peak value to decrease by nearly a third between $t = 1$ s to $t = 150$ s.

Figure 7(c) compares the period of the first linear vertical mode (as it evolves over the first 150 s) to the period of SAO. The mode-1 internal wave period clearly decreases, and the oscillation of the internal seiche thus accelerates over time; the decrease in period is due to the peak N^2 increasing in time. This process continues once the double-diffusive instability reaches its mature state over the whole domain. Note that the relative decrease of the mode-1 internal wave period serves as a "line of best fit" for the relative decrease in the period of SAO. Figure 8(c) shows the opposite, and instead the period increases in time as the peak N^2 value decreases. We once again see that the relative decrease of the mode-1 internal wave period serves as a "line of best fit" for the relative increase in the period of SAH.

C. Viscous dissipation

The viscous dissipation, $\epsilon = 2\rho_0 \nu e_{ij} e_{ij}$ (here e_{ij} is the rate of strain tensor), characterizes the irreversible conversion of mechanical energy to heat. Both the internal seiche motion (through shear across the pycnocline) and the small-scale double-diffusive instability (through shear along the filaments) contribute to the viscous dissipation, implying that this quantity has a strongly time-dependent nature. To demonstrate the spatiotemporal distribution of the viscous dissipation we have chosen to present Hovmöller plots of the horizontally averaged viscous dissipation. Since the mature double-diffusive instability occurs preferentially below the pycnocline, these allow for easy discrimination between the effects of the seiche, the effects of the mature double-diffusive instability and hybrid phenomena. The three different aspect ratio cases for a seiche with double diffusion are shown in Fig. 9(a) SAO, 9(b) DAO, and 9(c) QAO. It can be seen that a quasiperiodic pattern of viscous dissipation centered in the high shear region at the pycnocline is evident in all

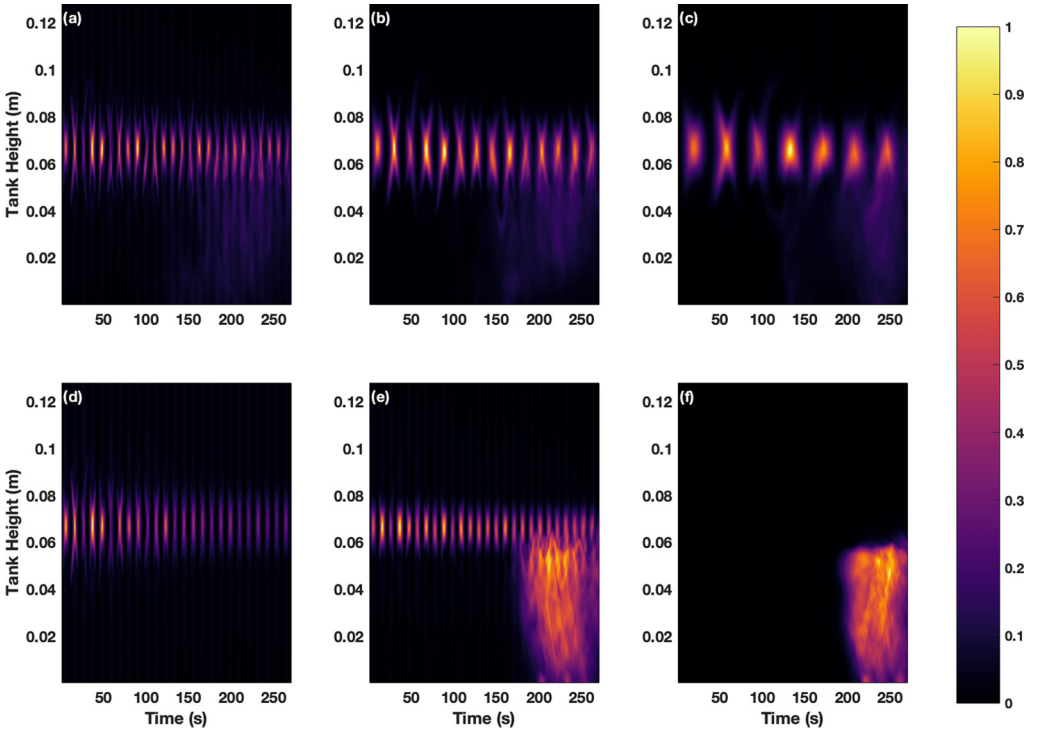

FIG. 9. The horizontally averaged viscous dissipation $\langle\epsilon\rangle_x$ as a function of z and t. Each panel has been scaled by the maximum viscous dissipation for the case shown, meaning that the geometric distribution of dissipation is highlighted. The panels show: (a) SAO with $\max\langle\epsilon\rangle_x = 1.054 \times 10^{-3}$ kg/(m s^3); (b) DAO with $\max\langle\epsilon\rangle_x = 8.680 \times 10^{-4}$ kg/(m s^3); (c) QAO with $\max\langle\epsilon\rangle_x = 8.431 \times 10^{-4}$ kg/(m s^3); (d) SAH with $\max\langle\epsilon\rangle_x = 8.259 \times 10^{-4}$ kg/(m s^3); (e) SaO with $\max\langle\epsilon\rangle_x = 2.832 \times 10^{-4}$ kg/(m s^3); and (f) SnO with $\max\langle\epsilon\rangle_x = 2.749 \times 10^{-4}$ kg/(m s^3).

cases–except the case without a seiche, SAN. Nonlinear effects lead to changes of shape in the seiche induced dissipation, with one prominent example being the "X-like" pattern for the second seiche period in Fig. 9(c). That is to say, viscous dissipation is spatially heterogeneous.

The onset of double-diffusive instability can be seen as a faint pattern below the pycnocline for all three cases, implying that seiche-induced dissipation dominates the instability induced dissipation. The cases in the bottom row of Fig. 9 differ from SAO as follows: Fig. 9(d) shows the case without double diffusion, SAH, Fig. 9(e) shows the case of a smaller amplitude seiche with double diffusion, SaO, Fig. 9(f) shows the case of no seiche and only double-diffusive instability, SnO. Comparing Figs. 9(a) and 9(d) shows that the early evolution appears to be similar with or without double diffusion. The case without double diffusion exhibits a faster relative decrease of viscous dissipation (though, recall these cases have been scaled to accentuate the spatial distribution of dissipation, hence a quantitative comparison of the rate of decay between cases will require a different figure). Figures 9(e) and 9(f) exhibit a far more prominent region of viscous dissipation below the pycnocline. Since Fig. 9(f) has only the double-diffusive instability, this region is clearly due to this instability. Interestingly, the plot in Fig. 9(e) shows that the effects of the small amplitude seiche are persistent well after the onset of the double-diffusive instability.

To better understand the magnitude of the viscous dissipation we define

$$\epsilon_c(t) = \int_0^t \left[\frac{1}{L_x L_z} \int_0^{Lx} \int_0^{Lz} \epsilon(x, z, s) dz dx \right] ds, \tag{16}$$

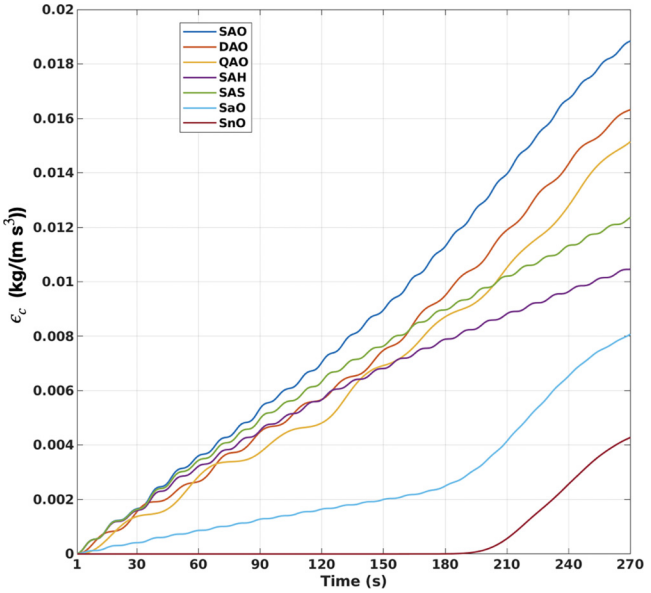

FIG. 10. The total energy dissipated up to a time t by the viscous dissipation.

which represents the domain-averaged dissipation of mechanical energy into heat, up to some time t. This quantity minimizes the quasiperiodic fluctuations due to the seiche motion yielding line graphs that are easier to interpret than just the total viscous dissipation at a given time. Figure 10 shows $\epsilon_c(t)$ for the cases SAO, DAO, QAO, SAH, SaO, and SnO. Note that undulations are present in the dissipation signal of each case except SnO. This is because the oscillations of a seiche create maxima and minima of shear along the pycnocline, thereby creating maxima and minima in the rate of viscous dissipation. Therefore, when the seiche is absent these undulations will be absent too.

A few conclusions can be drawn from this figure. The easiest to see is that the combined effects of the internal seiche and double-diffusive instability lead to more mean dissipation than either the pure double-diffusive instability, or the seiches without double diffusion (SAH and SAS); furthermore, the sum of final ϵ_c of SnO and SAS (or SAH) is less than the final ϵ_c of SAO. The second most obvious trend is that decreasing the aspect ratio (i.e., increasing the length of the seiche) leads to less mean dissipation within the same amount of time. To put this another way, as scale separation increases the efficiency of energy dissipation through viscous effects is decreased. However, even for the longest cases, the combined effects of seiches and double-diffusive instabilities dissipated more energy than both the single diffusion and pure instability cases. By comparing the SAO, SaO and SaN cases we can see that when the seiche amplitude is large the $\epsilon_c(t)$ versus t curve is linear to leading order. When the seiche amplitude is reduced, a clear kink is evident in this curve when the double-diffusive instability reaches its mature stage (after about $t = 180$ s). This kink is also observed in the seiche-free case (SnO). The energy dissipated after the onset of double-diffusive instability is slightly larger in the small amplitude seiche case (SaO).

IV. DISCUSSION

We have observed that internal seiches and double-diffusive instabilities can accelerate the timescales of specific facets of each other's development. The seiche modulates the double-diffusive instabilities as follows: the dispersion of the seiche generates mode-2 disturbances within the pycnocline which adjust the thermal and haline interface widths, which in turn affects the rate of formation of the unstable boundary layer and the subsequent production of filaments. Conversely,

the double-diffusive instability modulates the seiche as follows: the formation of the unstable boundary layer in turn increases the peak in N^2 across the pycnocline, which increases the frequency of oscillation of the seiche. Furthermore, the cumulative viscous dissipation (CVD) of a system with both a seiche and double-diffusive instabilities is greater than the sum of the CVD of an equivalent pure-seiche system and the CVD of an equivalent pure-double-diffusion system; that is, the currents corresponding to these disparate phenomena interact nonlinearly to dissipate kinetic energy.

To unambiguously establish these conclusions we used a thin-tanh stratification centered at middepth, and varied the tank aspect ratio. Though the parameter regime of the –O cases and the equation of state are representative of certain natural, geophysical systems, it is not immediately obvious how these results should scale to the field. We begin this discussion by noting that the experimental set-up of the seiche cases is not representative of naturally occurring stratifications, which are rarely (if ever) centered at middepth. We then describe how the results could extend to cases with longer horizontal extents, and taller vertical scales (i.e., as the ratio of the pycnocline width and the layer width shrink). We conclude the discussion section by noting the asymmetry in the growth of the double-diffusive instabilities above and below the pycnocline, and showing that this is due to the nonlinear equation of state.

A. Extension to the field-scale

We now present an example that is representative of internal waves observed in the field (where the pycnocline is typically not centered at middepth). In this case, the nonlinear seiche degenerates into wave trains. Figure 11 shows the Hovmöller plots of the vertically averaged kinetic energy for cases showing the degeneration into wavetrains. Case OSO with double diffusion is shown in Fig. 11(a), case OSH without double diffusion with $\kappa_s = \kappa_T = 1.43 \times 10^{-7}$ m$^2 \times$ s^{-1} is shown in Fig. 11(b), and case OSS without double diffusion with $\kappa_T = \kappa_s = 1.00 \times 10^{-8}$ m$^2 \times$ s^{-1} is shown in Fig. 11(c). After $t = 120$s each seiche has clearly degenerated into a wavetrain. During reflections, standing waves temporarily form near the reflecting wall. The time of the second reflection for each wavetrain is labeled. The wave train in the double-diffusive case OSO outpaces the wave train in OSS, which in turn outpaces the wave train in OSH. The differences in speed become visually discernible after $t = 195$ s in the corresponding supplemental video [40]. The root cause of the observed behavior is the same as the root cause of the increased frequency of the seiche in the cases with a pycnocline centered at the middepth: double diffusion causes the vertical N^2 profile to evolve into a narrower profile with a larger maximum [see Fig. 7(b)], and single diffusion leads to a broader N^2 profile with a lesser maximum [see Fig. 8(b)].

Figure 12 shows a snapshot of the wavetrain modified density field [Fig. 12(a)], and viscous dissipation [Fig. 12(b)]. The time chosen is after the first, and prior to the second, collision of the wavetrain with the walls ($t = 199$ s); that is, the wavetrain is traveling leftwards in this figure. The exact time was chosen for aesthetic reasons, though the behavior shown in the figure is generic. Figure 12(a) clearly shows three qualitatively different deformations of the pycnocline. The dominant feature is the wave train itself, with a leading wave that has the form of a solitary wave from exact, or DJL, theory [42]. The trailing waves are seen to depart somewhat from the clean form of the leading wave. The second prominent feature is a set of double-diffusive instabilities which form at the bottom of the pycnocline. Instabilities are seen to be prominent in the near wall regions, with reduced activity over the wave train. The third feature visible is a region with mature instabilities due to the collisions of the wave train with the right wall, and the self-interaction that follows collisions. Small wisps of overturning fluid are evident at, or just above, the top of the pycnocline in the same region. In turn, this advective instability instigates the double-diffusive instability below the pycnocline.

Figure 12(b) shows the viscous dissipation field. It can be seen that this is dominated by wave-induced shear, with the dominant feature caused by the leading wave in the wave train. The second and third waves induce viscous dissipation at a similar, or even slightly smaller level, as the post-collision, overturning region near the right wall. The double-diffusive instability below the

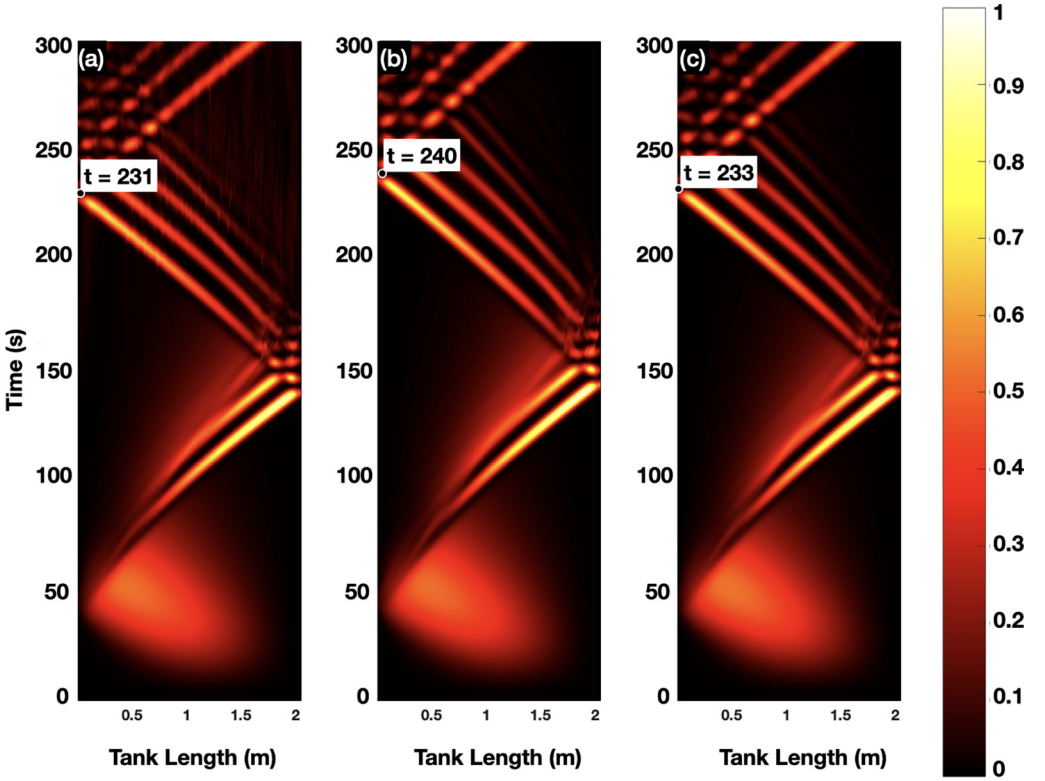

FIG. 11. Hovmöller plots of the vertically averaged kinetic energy density for cases with seiche degeneration into nonlinear, dispersive wave trains. (a) case OSO, (b) case OSH, and (c) case OSS. Each data set is normalized by its maximum value (OSO, 9.44×10^{-5} m^2/s^2; OSH 9.80×10^{-5} m^2/s^2; OSS 9.42×10^{-5} m^2/s^2). The onset of the double-diffusive instability corresponds to aberrations in the background state of panel (a).

pycnocline yields some viscous dissipation, with the filament-induced viscous dissipation below the overturning region near the right wall (which is furthest along in its evolution) being strongest at this time.

While differences between realistic and middepth stratifications do exist, many of the results observed in the main experiments hold true. Namely, double diffusion increases the wave speed by enhancing the buoyancy frequency via altering the stratification about the pycnocline; double-diffusive structures are more prominent near the walls than under the waves; and, enhanced viscous dissipation due to an accelerated wave speed and interactions between the wave-induced current and double-diffusive structures. A prominent difference is how the wave degeneration/self-interaction affects one of the mechanisms by which the wave modulates the instabilities. If the large structure is a seiche, mode-2 disturbances within the pycnocline cause local thinning and broadening of the pycnocline, which respectively excite and inhibit the instabilities; if the large structure is a wave-train, however, then overturning near the reflection point excites the instability by disturbing the unstable boundary layer instead. Mode-2 disturbances were not observed in the latter case.

While the simulations in this article were specifically designed so that they could be carried out in a reasonable physical laboratory setting, it is useful to briefly discuss the scale up the results to the field scale. First, note that the scale and growth rate of the instabilities is controlled by the

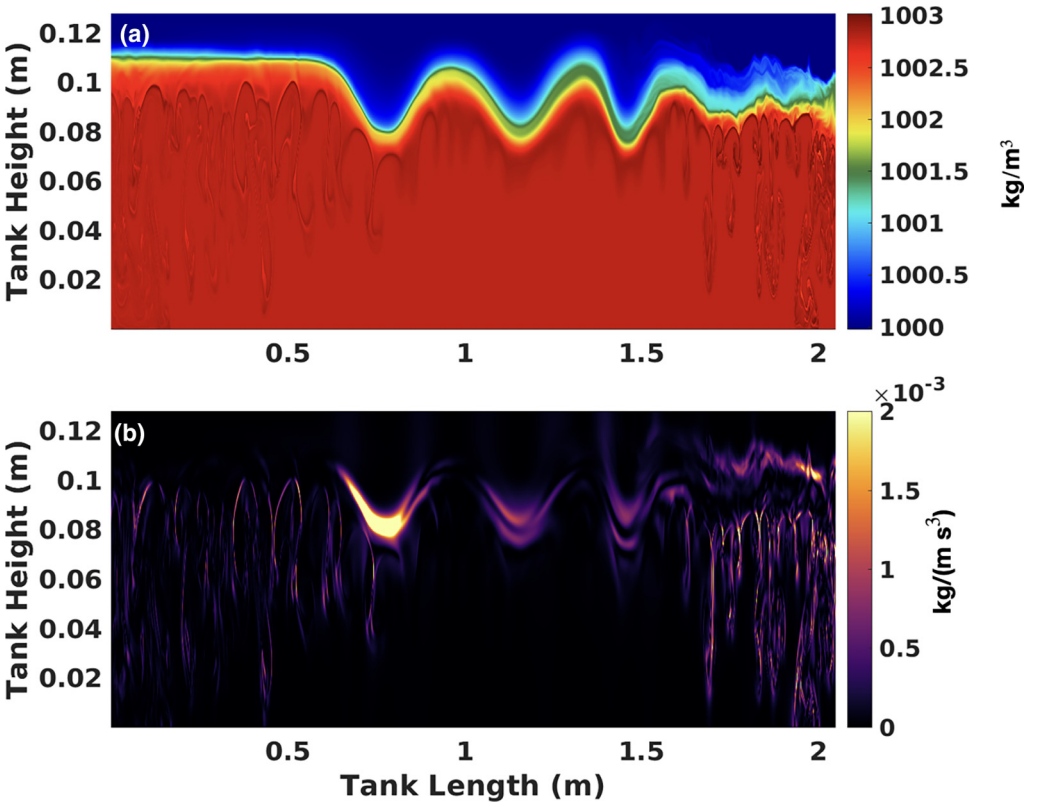

FIG. 12. Plots of (a) the density field and (b) the rate of viscous dissipation at time $t = 199$ s for the OSO case. As can be seen in the supplementary material, this is the wave after its first reflection, which was off of the right wall. The colormap for panel b) is saturated at 2.0×10^{-3} kg/(m s^3), but the maximum value in this field is 6.2×10^{-3} kg/(m s^3). The instability corresponds to filaments shed from beneath the pycnocline in a). In panel (b) viscous dissipation can be seen along the pycnocline and along these filaments. A mature shear instability is present above the pycnocline, on the right-hand side of panel (a).

ratio of the bulk change in S and the bulk change in T across the interface, τ,[8] and the ratio of the interface thicknesses of the vertical S and T profiles; they are thus not affected by the spatial scale of the domain. This is in complete contrast to internal waves, which have their time and length scales determined by the length and height of the domain, the initial wave amplitude, and the interface thickness in addition to the bulk change in density over the interface. In summary, if we fix viscosity, the initial interface width, bulk changes in T and S, and their diffusivities, then we should only see changes in the time and length scales of the internal wave as we change the height and width of the domain.

As mentioned in the Introduction, the diffusive-convection regime manifests in lakes and oceans as thermohaline staircases [24–26,28]. Measurements of temperature profiles from the Canadian Basin (CB) show staircase profiles with layers approximately 1–8 m thick ([24], Fig. 6(a)); microstructure measurements of temperature and chemical profiles from Lake Kivu (LK), show a mean layer width of 8 m ([26], Table 1). This gives two characteristic length scales: the height

[8]That is, the ratio of the diffusivity of salt to the diffusivity of heat.

of the domain, H_D, or the height of a layer in the staircase, H_L.[9] The mean interface width from LK was about 2% the mean H_L, and about 0.04% the profile H_D. The initial interface width in this investigation is about 7.8% of the characteristic height, so we can therefore reasonably expect results to carry over to the field if we use the layer width as the characteristic height in our present analysis.

Now, suppose a wave train of horizontal extent $O(H_L)$ and amplitude $O(0.1H_L)$ (such as the waves used in this investigation) travels along one interface within the staircase shortly after it is generated locally. Since these natural staircases are thermally forced, we can expect molecular heat flux and active unstable boundary layer formation to be present. Thus, this wave will accelerate as it travels through the staircase. One complication is that it will begin to generate waves in the adjacent interfaces [19], but we can expect this collection of coupled waves to travel faster than if they were in an analogous, singly diffusive or nondiffusive stratification. We can also expect them to continue accelerating as long as boundary layer formation is present.

As noted earlier, these internal wave trains may not produce the same mode-2 disturbances as a seiche; nevertheless, they can still modulate the double-diffusive instability via shear instabilities produced during the evolution of the wave [18]. Shear instabilities can disturb the unstable boundary layer, and even induce overturning, which we know accelerates the generation of filaments from the discussion of Fig. 12. Referring to Fig. 7(d) of Grace *et al.* [18], we see that other shear instabilties can locally increase the interface thickness; this would decrease molecular heat flux across the interface and thereby inhibit formation of unstable boundary layers and filaments. In fact, by inducing waves in adjacent interfaces, large amplitude (say $\sim 0.5H_L$) wave trains with a large horizontal extent (say $\sim 20H_L$) could feasibly generate localized traveling patches of modulated heat flux within a staircase.

B. The nonlinear equation of state

In the –O parameter regime of this investigation, we observed only downward-growing filaments. To ensure that this was not a numerical artifact, we re-ran the SAO case using the original equation of state (6) linearized about the midpoints of the initial ranges of the temperature and salinity fields (calculated by $\frac{T_0+\Delta T}{2}$ and $\frac{S_0+\Delta S}{2}$, respectively). Figure 13 depicts the density field of the linear-equation-of-state-SAO case at $t = 495$s; clearly, the growth of the filaments is symmetric when the equation of state is linear. Interestingly, the onset of the instability is much slower in the system governed by a linear equation of state.

This is in agreement with the investigation of Özgökmen and Esenkov [32] into the effect of a quadratic (in temperature) equation of state on the growth of salt-fingers. They found that-compared to a system governed by a linear equation of state—a strongly nonlinear equation of state leads to highly asymmetric development of salt fingers. As can be seen in their Fig. 6, only downward-growing fingers are observed in the density field of the strongly nonlinear case, whereas both upward-growing and downward-growing fingers (of the same size) are observed in the density field of the linear case [32]. Thus, a nonlinear equation of state leads to the asymmetric growth of instability-induced structures in both the salt-finger and diffusive-convection regimes of double-diffusive instabilities.

V. CONCLUSIONS AND FUTURE WORK

Based on the results presented above we can draw several conclusions. First, we see that the presence of a seiche accelerates the maturation of the double-diffusive instability. Small, convex, mode-2 waves generated by the nonlinear dispersion of the seiche distend the unstable layer, thereby

[9]We ignore the horizontal scale of the staircase, since internal waves can be locally generated via the degeneration of large internal waves or via local biological, geological, or physical events.

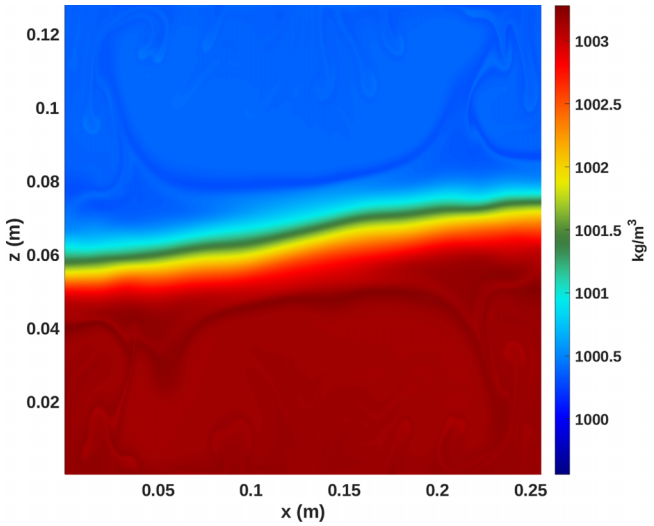

FIG. 13. The density field at $t = 495$ s of SAO re-run using the equation of state (6) linearized about the initial initial midpoints of the temperature and salinity distributions.

allowing the currents of the seiche to deform it into a filament (see Fig. 4(a) and the Supplemental Material [40]; also refer to a sketch of this mechanism in Fig. 14). Similarly, small, concave, mode-2 waves locally decrease the width of the T and S interfaces, which expedites the growth of the unstable boundary layer in concentrated regions immediately below the pycnocline.

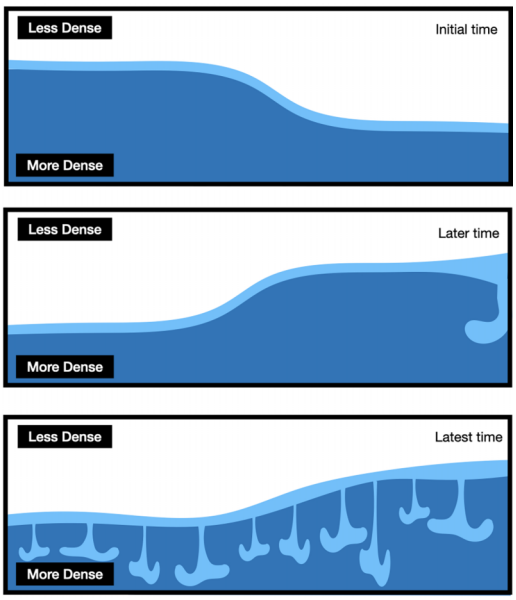

FIG. 14. The process of filament formation in the presence of a nonlinear seiche. In the middle panel we see early local growth, which is due to localized pycnocline (and thus halocline and thermocline) thinning by higher harmonic and higher mode waves. In the bottom panel we eventually see global filament growth. Global filament growth is slightly accelerated due to the shear generated by the seiche.

Second, we observe that double diffusion accelerates the dynamics of the seiche by altering the background stratification [i.e., $\bar{\rho}$ in Eq. (12)]. As a result of the instability, a statically unstable layer forms beneath the pycnocline before the filaments begin to grow; the stratification about the pycnocline then changes so the N^2 has a narrower profile with a greater maximum relative to the initial profile (at a given x value). Refer to Fig. 7(b) for visual example.

Finally, we find that both shear along the pycnocline (produced by the seiche), and that along filaments (as they move against the current) significantly and distinctly contribute to the overall dissipation of energy. It is important to note that we say "distinctly" and not "independently"; for, as can be seen in Fig. 10, the total energy dissipated by SnO added to what is dissipated by SAH does not sum to the total energy dissipated by SAO. This implies that the seiche and the instability act in tandem to dissipate energy. To see how they do so, consider the unstable layer immediately before filaments form. The fluid particles in this region have a horizontal momentum determined by the seiche-induced velocity. As a filament forms, these particles sink. As they sink, they encounter currents increasingly greater in magnitude; these fluid particles therefore experience greater shear (and dissipation) than if they had remained at their original locations (such as in the SAH case). Likewise, the additional momentum imparted to filaments by the seiche allows them to move faster than if they were solely accelerated by buoyant forces, which allows for greater dissipation than in the SnO case.

Future work could extend the simulations presented here to three-dimensions, likely focusing on the propagating wave trains. An alternative option, and one in which we have made some preliminary explorations, is to consider the salt fingering regime of double-diffusive instability. This regime is expected to yield a stronger interaction between the instability and the seiche, and will offer a counterpoint to the scale separation presented in this article.

In conclusion we have quantified the behavior of a wave-instability system that exhibits scale separation using high-resolution numerical simulations. The simulations shown were on the scale of laboratory experiments, though the scale separation that would occur in nature would be even larger. Scale separation implies that the interaction between the instability and seiche allows each to evolve in a modulated form of that would not be realized when either an internal seiche or double-diffusive instability is simulated on its own. Nevertheless, the interaction does exist, and should be readily measurable in the laboratory. Moreover, the nature of the interaction is different from the classical turbulent energy cascade in the inertial regime: the kinetic energy of the large-scale seiche directly accelerates the onset of motion, and therefore the activation of kinetic energy, at the small length scales associated with the double-diffusive instability.

ACKNOWLEDGMENTS

This research project was funded by the Natural Sciences and Engineering Research Council of Canada (NSERC) Discovery Grant RGPIN-311844-37157. The constructive comments of the anonymous reviewers significantly improved the paper.

[1] P. A. Davidson, *Turbulence: An Introduction for Scientists and Engineers* (Oxford University Press, Oxford, UK, 2015).

[2] J. C. Wyngaard, *Turbulence in the Atmosphere* (Cambridge University Press, Cambridge, UK, 2010).

[3] O. M. Phillips, *The Dynamics of the Upper Ocean* (Cambridge University Press, Cambridge, UK, 1966).

[4] A. C. Newell and B. Rumpf, Wave turbulence, Annu. Rev. Fluid Mech. **43**, 59 (2011).

[5] K. G. Lamb and V. T. Nguyen, Calculating energy flux in internal solitary waves with an application to reflectance, J. Phys. Oceanogr. **39**, 559 (2009).

[6] C. Xu and M. Stastna, On the interaction of short linear internal waves with internal solitary waves, Nonlin. Process. Geophys. **25**, 1 (2018).

[7] M. Dunphy and K. G. Lamb, Focusing and vertical mode scattering of the first mode internal tide by mesoscale eddy interaction, J. Geophys. Res. Oceans **119**, 523 (2014).
[8] M. Dunphy, A. L. Ponte, P. Klein, and S. Le Gentil, Low-mode internal tide propagation in a turbulent eddy field, J. Phys. Oceanogr. **47**, 649 (2017).
[9] E. Kunze, Near-inertial wave propagation in geostrophic shear, J. Phys. Oceanogr. **15**, 544 (1985).
[10] C. Chavanne, P. Flament, D. Luther, and K. Gurgel, The surface expression of semidiurnal internal tides near a strong source at Hawaii. Part II: Interactions with mesoscale currents, J. Phys. Oceanogr. **40**, 1180 (2010).
[11] M. McIntyre, Potential-vorticity inversion and the wave-turbulence jigsaw: Some recent clarifications, Adv. Geosci. **15**, 47 (2008).
[12] M. Preusse, F. Peeters, and A. Lorke, Internal waves and the generation of turbulence in the thermocline of a large lake, Limnol. Oceanogr. **55**, 2353 (2010).
[13] I. Ostrovsky, Y. Z. Yacobi, P. Walline, and I. Kalikhman, Seiche-induced mixing: Its impact on lake productivity, Limnol. Oceanogr. **41**, 323 (1996).
[14] L. Boegman, J. Imberger, G. N. Ivey, and J. P. Antenucci, High-frequency internal waves in large stratified lakes, Limnol. Oceanogr. **48**, 895 (2003).
[15] L. Boegman, G. Ivey, and J. Imberger, The energetics of large-scale internal wave degeneration in lakes, J. Fluid Mech. **531**, 159 (1999).
[16] D. Horn, J. Imberger, and G. Ivey, The degeneration of large-scale interfacial gravity waves in lakes, J. Fluid Mech. **434**, 181 (2001).
[17] H. Michallet and E. Barthelemy, Experimental study of interfacial solitary waves, J. Fluid Mech. **366**, 159 (1998).
[18] A. Grace, M. Stastna, and F. J. Poulin, Numerical simulations of the shear instability and subsequent degeneration of basin scale internal standing waves, Phys. Rev. Fluids **4**, 014802 (2019).
[19] P. F. Kundu and I. M. Cohen, *Fluid Mechanics*, 4th ed. (Elsevier, Amsterdam, 2004).
[20] W. D. Smyth and J. R. Carpenter, *Instability in Geophysical Flows* (Cambridge University Press, Cambridge, UK, 2019).
[21] H. Stommel, A. B. Arons, and D. Blanchard, An oceanographical curiosity: The perpetual salt fountain, Deep Sea Res. (1953) **3**, 152 (1956).
[22] M. E. Stern, The "salt-fountain" and thermohaline convection, Tellus **12**, 172 (1960).
[23] J. Turner and H. Stommel, A new case of convection in the presence of combined vertical salinity and temperature gradients, Proc. Natl. Acad. Sci. USA **52**, 49 (1964).
[24] N. C. Shibley, M.-L. Timmermans, J. R. Carpenter, and J. M. Toole, Spatial variability of the arctic ocean's double-diffusive staircase, J. Geophys. Res. Oceans **122**, 980 (2017).
[25] R. W. Schmitt, Double diffusion in oceanography, Annu. Rev. Fluid Mech. **26**, 255 (1994).
[26] M. Schmid, M. Busbridge, and A. Wüest, Double-diffusive convection in Lake Kivu, Limnol. Oceanogr. **55**, 225 (2010).
[27] T. Radko, Thermohaline layering in dynamically and diffusively stable shear flows, J. Fluid Mech. **805**, 147 (2016).
[28] D. Kelley, H. Fernando, A. Gargett, J. Tanny, and E. Özsoy, The diffusive regime of double-diffusive convection, Prog. Oceanogr. **56**, 461 (2003).
[29] J. S. Turner, The melting of ice in the arctic ocean: The influence of double-diffusive transport of heat from below, J. Phys. Oceanogr. **40**, 249 (2010).
[30] C. Subich, *Simulation of the Navier-Stokes Equations in Three Dimensions with a Spectral Collocation Method* (University of Waterloo, Ontario, Canada, 2011).
[31] D. Brydon, S. Sun, and R. Bleck, A new approximation of the equation of state for seawater, suitable for numerical ocean models, J. Geophys. Res. **104**, 1537 (1999).
[32] T. M. Özgökmen and O. E. Esenkov, Asymmetric salt fingers induced by a nonlinear equation of state, Phys. Fluids **10**, 1882 (1998).
[33] J. R. Carpenter, T. Sommer, and A. Wüest, Simulations of a double-diffusive interface in the diffusive convection regime, J. Fluid Mech. **711**, 411 (2012).

[34] J. Turner, The coupled turbulent transports of salt and and heat across a sharp density interface, Int. J. Heat Mass Transf. **8**, 759 (1965).
[35] D. E. Kelley, Fluxes through diffusive staircases: A new formulation, J. Geophys. Res. Oceans **95**, 3365 (1990).
[36] J. Carpenter, T. Sommer, and A. Wüest, Stability of a double-diffusive interface in the diffusive convection regime, J. Phys. Oceanogr. **42**, 840 (2012).
[37] M. Hieronymus and J. R. Carpenter, Energy and variance budgets of a diffusive staircase with implications for heat flux scaling, J. Phys. Oceanogr. **46**, 2553 (2016).
[38] J. D. Flanagan, A. S. Lefler, and T. Radko, Heat transport through diffusive interfaces, Geophys. Res. Lett. **40**, 2466 (2013).
[39] A. de la Fuente, K. Shimizu, Y. Niño, and J. Imberger, Nonlinear and weakly nonhydrostatic inviscid evolution of internal gravitational basin-scale waves in a large, deep lake: Lake constance, J. Geophys. Res. Oceans **115**, 2009JC005839 (2010).
[40] See Supplemental Material at http://link.aps.org/supplemental/10.1103/PhysRevFluids.8.034801 for movies depicting the evolution of the salinity and density fields.
[41] A. P. Stamp, G. O. Hughes, R. I. Nokes, and R. W. Griffiths, The coupling of waves and convection, J. Fluid Mech. **372**, 231 (1998).
[42] K. G. Lamb, Are solitary internal waves solitons? Stud. Appl. Math. **101**, 289 (1998).